42th AIAA Plasmadynamics and Lasers Conference AIAA-2011-3280
27 – 30 Jun 2011, Honolulu, HI

Flight Measurements of Aero-Optical Distortions from a Flat-Windowed Turret on the Airborne Aero-Optics Laboratory (AAOL)

Chris Porter[1], Stanislav Gordeyev[2], Mike Zenk[3], and Eric Jumper[4]
University of Notre Dame, Notre Dame, Indiana, 46545

The optical environment of a flat-window hemisphere-on-cylinder turret during flight tests in Notre Dame's Airborne Aero-Optics Laboratory was evaluated. Aero-optical aberrations around the turret were measured using a high-speed (up to 20 kHz) Shack-Hartmann wavefront sensor providing the most complete aero-optical mapping to date. The primary data was acquired at Mach 0.5 at an altitude of 15,000 ft, with a subset of the data collected at Mach 0.4 for verification of scaling relationships. During each flight, data were acquired holding the elevation/azimuthal angle of the aperture constant. Additional data sets were acquired allowing the two planes to slew by, providing statistical data over a large range of aperture angles. The flight test data were also compared to wind tunnel measurements using the identical turret. Finally, using the spatial statistics of the flight data, the use of the Large Aperture Approximation (LAA) to estimate the resulting time-averaged far-field Strehl ratio is revisited.

Nomenclature

A_D = aperture diameter
Az = azimuthal angle
E = expectation operator
El = elevation angle
I = irradiance
I_0 = diffraction-limited irradiance
K_{GD} = Gladstone-Dale constant
n = index of refraction
OPD = optical path difference
OPL = optical path length
SR = Strehl ratio
t = time
$\boldsymbol{x}$ = position vector
x,y = aperture coordinates
X = random variable
z = far-field distance
α = viewing angle
β = modified elevation angle
γ_1 = skewness
γ_2 = excess
σ = standard deviation
μ = moment about the mean
ρ = density
λ = wavelength
ν = local speed of light
ϕ = characteristic function
s = integration variable

---

[1] Graduate Student, Department of Mechanical and Aerospace Engineering, Hessert Laboratory for Aerospace Research, Notre Dame, IN 46556, Student Member.

[2] Research Associate Professor, Department of Mechanical and Aerospace Engineering, Hessert Laboratory for Aerospace Research, Notre Dame, IN 46556, Senior AIAA Member.

[3] Project Manager, Department of Mechanical and Aerospace Engineering, Hessert Laboratory for Aerospace Research, Notre Dame, IN 46556, AIAA Member.

[4] Professor, Department of Mechanical and Aerospace Engineering, Hessert Laboratory for Aerospace Research, Notre Dame, IN 46556, AIAA Fellow.

I. Introduction

IN the late 1970s and early 1980s optical turrets where extensively studied as the use of lasers on aircraft started to become feasible. During this period, the Airborne Laser Laboratory (ALL) successfully demonstrated the usefulness of airborne lasers [1], although it was deemed impractical at the time. The ALL carbon dioxide laser's long wavelength (10.6 μm) limited the range and irradiance that the system could deliver on target. As laser technology and adaptive-optics systems improved, the use of lasers for directed energy and communication applications was revived. With new more powerful lasers came the ability to deliver more laser energy onto a target and an increased range. However, the shorter wavelength (1-1.5 μm) of new lasers increased the detrimental effects that inhomogeneous refractive mediums [2-4] have on the ability of optical systems to focus a laser beam in the far-field.

With the new potential of these lasers, achieving a maximum field-of-regard is a necessity. To obtain a full field-of-regard, hemisphere-on-cylinder turrets offer a simple, mechanically efficient means to project or receive laser radiation to or from a target [5]. However, the flow around a turret consists of a separated wake region aft of the turret where pressure and temperature fluctuations result in density and index-of-refraction fluctuations. These fluctuations result in beam jitter (bore-sight error) and higher-order aberrations that reduce the peak irradiance of the laser beam in the far-field. Therefore, aero-optical effects can severely limit an airborne directed-energy system's field-of-regard. To verify wind tunnel experiments [6, 7] and computational simulations [8-11], aero-optical measurements measured under realistic flight conditions are needed. Yet, to the author's knowledge, there is no open literature flight tests data available to perform the comparison. The Airborne Aero-Optics Laboratory (AAOL) [12] reverses this shortfall by adding flight test capabilities as a viable and affordable experimental tool. This tool not only advances the scientific exploration of aero-optic effects, but also allows for real-flight studies of various mitigation schemes involving flow control and adaptive optics.

The AAOL flight program consists of two Citations flying in formation approximately 50 m apart to minimize atmospheric effects. A diverging, small-diameter, continuous laser beam is sent from a chase plane to an airborne laboratory, see Fig. 1. The flight-test airborne laboratory consists of a one-foot-diameter turret with a four-inch flat-window aperture extruding out the side of the Citation's escape hatch to receive the incoming laser beam. Once the laser and turret systems are tracking each other, the beam is sent through a series of optics resulting in a collimated-planar wavefront under ideal conditions. A fast-steering mirror stabilizes the beam to reduce the overall beam jitter. After the fast-steering-mirror system, the beam exits the turret assembly onto an optical table onboard the AAOL aircraft and is sent to a suite of sensors.

Figure 1: Notre Dame's Airborne Aero-optics Laboratory. Left) Two Citations flying in formation to measure the aero-optics effects of the flow around a turret. Right) Picture taken during the first flight test of the laser on the turret.

Given the complexity of both the flow field and experimental setup to measure the aero-optic effects around optical turrets, many fundamental studies have been performed by concentrating on the predominant flow features surrounding a turret, such as separated shear layers [13-16] and turbulent boundary layers [17-19]. Experimental optical data on flat-windowed turrets is limited [7]; to obtain relevant optical data requires facilities large enough for pertinent Reynolds and Mach number flows with optical access. Structural interference from wind tunnels with these capabilities still limits the achievable aperture angles where optical data can be acquired. As such, AAOL represents a unique capability to obtain flight data over a range of azimuthal/elevation angles at subsonic and low transonic speeds while simultaneously eliminating tunnel-blockage and interference effects.

The following paper provides a short background on the fluid dynamics of hemisphere-on-cylinder turrets (Section IIA) and the coupling of fluid-dynamical and aero-optical effects (Section IIB). The experimental setup for the flight tests is discussed in Section III. Section IV presents the optical results from several flights, verifies previously proposed scaling relationships, presents complementary wind tunnel tests and revisits the Large Aperture Approximation's applicability to aero-optic aberrations. The conclusions are discussed in Section V.

II. Background

A. Fluid Dynamics of Turrets

The flow around a hemisphere-on-cylinder turret is highly complex and three-dimensional [5, 20]. The dynamics of the flow field depends upon both the Reynolds number and Mach number. Still, a few general flow features are apparent for most Reynolds number and low-subsonic Mach number tests. A full description of the current understanding of the wake region around the turret based on different tunnel experiments and CFD simulations is presented in a recent review paper [5], and illustrated in Fig. 2.

At the front of the turret, a necklace vortex forms near the base, extends along the sides of the turret, and continues on in the downstream direction aft of the turret. On the upstream half of the turret, the flow remains attached and an inviscid approximation generally well describes the flow field. The flow is forced to accelerate as it goes around and over the turret with a favorable pressure gradient on the upstream half of the turret. At the aft portion of the turret, the flow experiences an adverse pressure gradient and separates at some point. The location of the separation point and the downstream wake characteristics are dependent on the Reynolds number. As the flow separates creating a shear layer, coherent vortical structures form and eventually roll up into two large "horn" vortices. The low pressure and associated low density inside these vortical structures result in a spatially- and temporally-varying index-of-refraction field, thus creating a non-ideal optical environment.

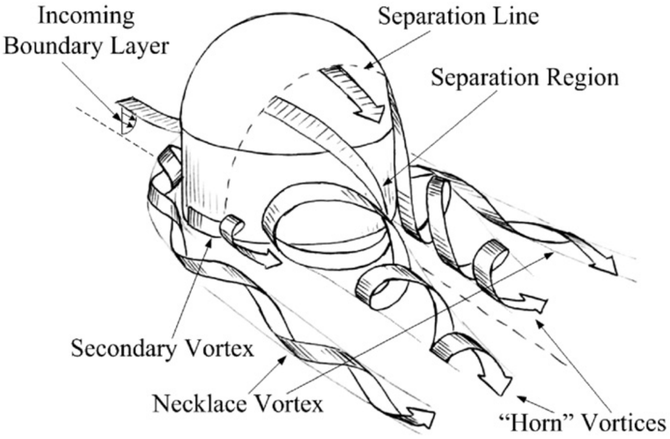

Figure 2: Schematic of the subsonic flow around a turret [5].

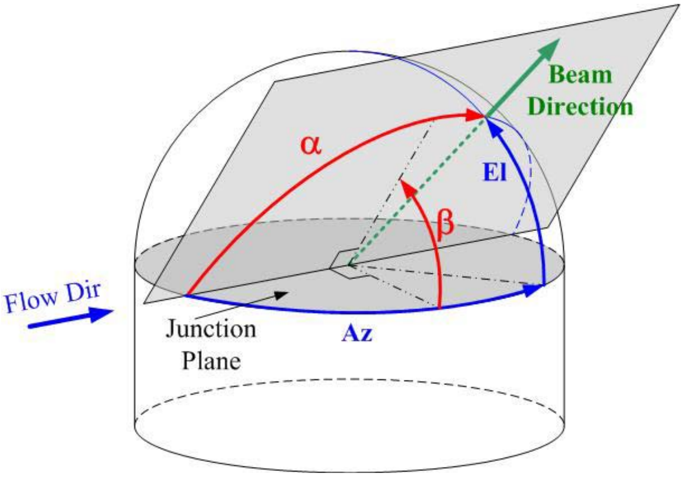

Figure 3: Definition of angles to describe the beam direction

Depending on the azimuthal (*Az*) and elevation (*El*) angles, the beam entering or exiting the aperture of the turret propagates through some of these different regions of the flow field, see Figure 3. The location of the aperture is most commonly described using the azimuthal/elevation angle coordinate system. However, from a flow-physics point of view, it is more convenient to introduce a different coordinate system to describe the beam direction. This coordinate system uses the viewing angle, α, and the modified elevation angle, β, to define the direction of the beam, see Figure 3. The viewing angle, α, is defined as the angle between the flow direction and beam direction vectors. The modified elevation angle, β, is defined as the angle between the junction plane joining the hemisphere to the cylinder and the plane formed by the flow direction and the beam direction vectors. These angles are related to the azimuthal and the elevation angles through the following relations:

$$\alpha = \cos^{-1}(\cos(Az)\cos(El))$$
$$\beta = \tan^{-1}\left(\frac{\tan El}{\sin Az}\right). \tag{1}$$

To show the physical reasoning for this coordinate system, note that for the flow around a sphere, time-averaged flow quantities are a function of the viewing angle, α, only. Therefore, the modified elevation angle accounts for the presence of the cylindrical portion of the turret and the ground effects caused by the wall the turret is mounted on. The effect of the flat-window aperture on the asymmetry of the flow field will also be seen in the modified elevation angle.

B. Coupling the Fluid Dynamics and Optical Analysis

As mentioned before, the unsteady wake generated by the flow around the hemisphere-on-cylinder turret results in pressure, temperature, and density fluctuations. Through the Gladstone-Dale constant, the density and the index-of-refraction are related by,

$$n(\boldsymbol{x},t) - 1 = K_{GD}\,\rho(\boldsymbol{x},t). \tag{2}$$

Since the index-of-refraction field is a function of both space and time, the speed at which light propagates through the turbulent medium is also a function of both space and time. Therefore, when a planar wavefront propagates through a spatially- and temporally-varying density field, the wavefront emerges distorted, reducing the ability of the beam to focus to a spot in the far-field.

Aberrations, or phase differences imposed on the beam result from some portions of the wavefront traveling farther over a given time period then others due to the spatially-varying local index-of-refraction they propagate through. Given the index-of-refraction field, the optical path length, *OPL*, is calculated as

$$OPL(\boldsymbol{x},t) = \int_{s1}^{s2} n(\boldsymbol{x},t)ds, \tag{3}$$

although the deviation from the spatially-averaged mean, or the Optical Path Difference, *OPD*, is the primary concern,

$$OPD(\boldsymbol{x},t) = OPL(\boldsymbol{x},t) - \overline{OPL}(\boldsymbol{x},t). \tag{4}$$

In Eq. 4, the over-bar represents the spatially-averaged optical path length over the aperture, **x**, at a given time, *t*. To characterize the effect that changes in OPD across the aperture have on the far-field, the instantaneous Strehl ratio (SR) is determined. The Strehl ratio is the ratio of the on-axis irradiance, *I*, to the diffraction-limited on-axis irradiance, I_0. When the spatial probability distribution of the phase error is Gaussian at every instant, then the *exponential* form of the Maréchal approximation, [2],

$$SR(t) = \frac{I}{I_0} = e^{-\left(\frac{2\pi OPD_{RMS}(t)}{\lambda}\right)^2} \tag{5a}$$

accurately predicts the instantaneous Strehl ratio. In Eq. (5a), the $\mathrm{OPD_{RMS}}$ is the spatial variance of the OPD over the aperture. Steinmetz [21] showed that in the limit when the aperture size is much larger than the turbulence structure size, the so-called Large Aperture Approximation (LAA, Eq. (5b)), the Maréchal approximation is approximately valid for any processes for the time-averaged Strehl ratio, if the time-averaged $\mathrm{OPD_{RMS}}$ is used,

$$\overline{SR} \approx e^{-\left(\frac{2\pi \overline{OPD}_{RMS}}{\lambda}\right)^2}. \tag{5b}$$

In general, for wavefronts with arbitrary distributions, the Fraunhofer approximation must be used to provide accurate Strehl ratio results,

$$SR(t) = \frac{\left(\left|\iint e^{i\frac{2\pi}{\lambda z}OPD(x,y,t)}dxdy\right|\right)^2}{\left(\iint dxdy\right)^2}. \tag{6}$$

III. Experimental Setup

The Airborne Aero-Optics Laboratory consists of two planes flying in closed formation. The main data-acquisition aircraft (the Airborne Aero-Optics Laboratory itself) is integrated with the turret and instrumentation, which is complemented by the chase aircraft (laser source aircraft). During the data acquisition process, the chase plane sends a diverging beam that overfills the turret's aperture on the main aircraft by approximately a factor of two. The beam passes through the flat-window aperture of the turret, Figure 4, through a set of optics to reduce the beam diameter from the 0.1016 m diameter of the physical aperture to 0.020 m. After the beam diameter has been reduced, a fast steering mirror is used to stabilize the beam coming out of the turret assembly onto the optical bench where it is sent to a suite of instruments, see Figure 5.

Figure 4: Pictures of the turret mounted on the Citation with a schematic of the turret assembly and shell of the aircraft.

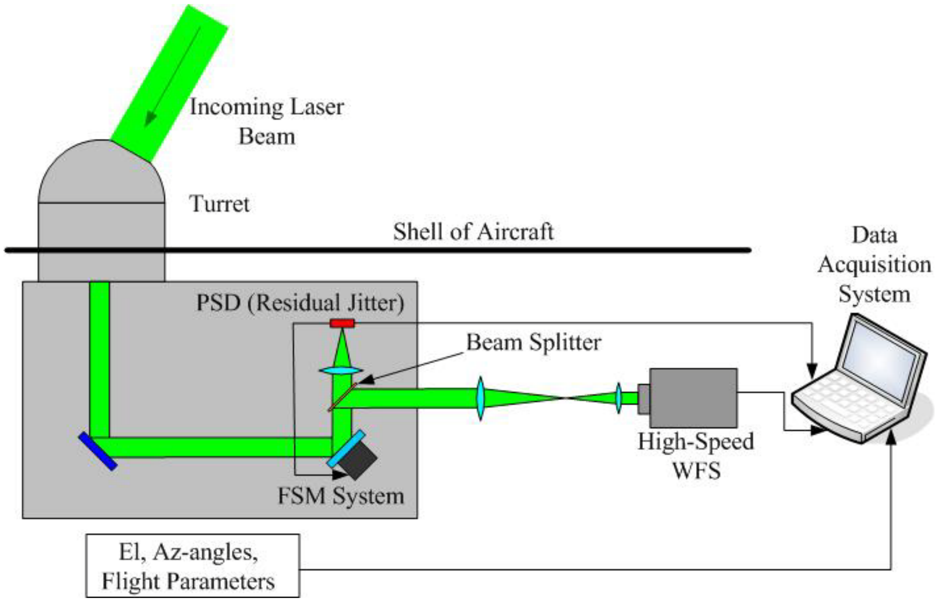

Figure 5: Optical setup of the beam path and suite of instruments during flight tests.

For the data presented in this paper, the beam was sent to a high-speed Shack-Hartmann wavefront sensor through a set of relay optics to reimage the beam onto the sensor. At full resolution, the Shack-Hartmann sensor used is capable of acquisition rates up to 5 kHz with a spatial resolution of 61x71 lenslets. However, for the majority of the tests, the spatial resolution was reduced to approximately 32x32 lenslets, allowing for an increased frame rate of 20 kHz. To minimize spatial smearing, the camera's aperture time was set for 0.5 μs. Finally, during the processing of the wavefronts, all steady-lensing aberrations along with the instantaneous piston and tip/tilt were removed from each wavefront leaving only higher-order aberrations.

In addition to the high-speed wavefront measurements, Figure 5 also shows the schematic of additional measurements made during flights. After the fast steering mirror (FSM), the beam was split by a beam splitter and sent to a Position Sensing Devices (PSD), which measured the residual jitter in the beam after the FSM. Simultaneously, the instantaneous azimuthal and elevation angles of the turret were recorded throughout each flight. Depending on the flight setup, additional parameters are also available to be recorded. During these flights, a boundary-layer Pitot-rake was installed below the turret to record the total and static pressures in the freestream to calculate the Mach number.

All wavefront measurements were performed with the planes flying at an altitude of 15,000 ft at a Mach number of either 0.4 or 0.5. Once the planes were in formation and the turret and laser systems were tracking each other, wavefront data acquisition began. At this point, either fixed-angle data or slewing data were acquired. For the fixed-angle data, the pilots positioned the aircraft such that the flat-window aperture was pointing at a specific azimuthal/elevation angle when tracking the laser. The wavefront sensor acquired data at the 20-kHz frame rate for a sampling time of 0.5 seconds (10,000 wavefronts).

For the slewing data, the frame rate of the camera was reduced to 3 kHz to increase the sampling time to 14.3 seconds. During this time interval, the chase plane reduced its speed so that the azimuth/elevation angles between the two planes slowly and monotonically changed. An example of the time record of the azimuthal/elevation angles during a slewing maneuver is shown in Figure 6. The elevation angle during this maneuver remained primarily constant, while the azimuthal and the viewing angles increased almost monotonically by 15-20 degrees. During each slewing maneuver, 43,240 wavefronts were recorded. For the analysis, each dataset was split into sequential subsets of 3,000 wavefronts (one-second subsets). For each subset, the time-averaged wavefront and the instantaneous tip/tilt were removed and instantaneous spatial statistics, such as the spatial OPD_{RMS}, were calculated. For each one-second subset, the corresponding time-averaged azimuthal and elevation angles of the flat-windowed aperture were recorded.

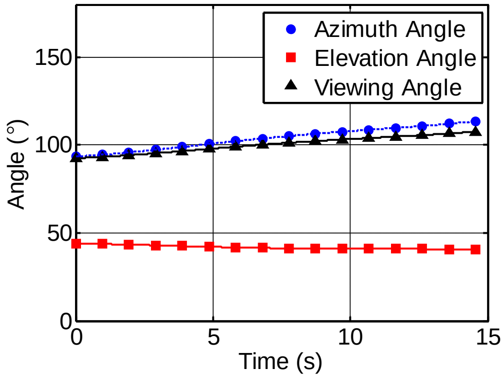

Figure 6. Example of the instantaneous azimuth, elevation, and viewing angles of the turret during a slewing maneuver.

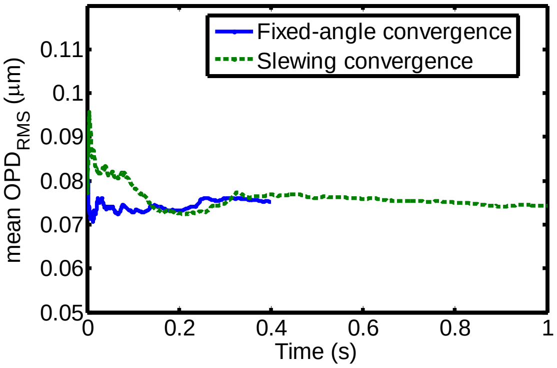

Figure 7. Convergence of the mean spatial OPD_{RMS} of a fixed-angle test and the one-second subset of a slewing maneuver corresponding to the same azimuthal and elevation angles.

Typical flow time scales around a turret at these Reynolds and Mach numbers are on the order of a few milliseconds, while the angular rate of rotation of the turret during a slewing maneuver is on the order of a degree per second. Therefore, at every moment the flow quickly adjusts to the slow-changing aperture location and the optical statistics (i.e. average OPD_{RMS}) were not affected by the rotation of the turret; thus, the slewing maneuvers allowed for a rapid mapping of the aero-optic environment around the turret yielding a large amount of statistical data over a range of azimuthal and elevation angles. To verify that the rotation of the turret during the data acquisition process did not influence the optical statistics, Figure 7 shows the convergence of the mean spatial OPD_{RMS} of a fixed-angle dataset and the corresponding subset of a slewing maneuver at the same azimuthal/elevation angles. Only a small 1%-difference exists between the converged mean of the fixed-angle test and subset of the slewing maneuver; similar results were observed for other data sets investigated. Therefore, statistically breaking up the slewing data into small subsets of data is equivalent to acquiring a series of fixed-angle data points. Finally, in Section IV, it will also be shown that even the calculated higher-order statistics (at least up to the fourth moment) are very similar between fixed-angle and slewing subsets. Therefore, in the remainder of this paper no distinction will be made between the fixed-angle and slewing-maneuver data.

IV. Results

A. Flight Data

To gain a better understanding of the aero-optic environment around the flat-windowed turret, time-averaged levels of aero-optical distortions, OPD_{RMS}, over a large range of azimuthal and elevation angles were measured. Figure 8A shows the locations of all the elevation/azimuthal points (gray dots) where aero-optical distortions were measured. Figure 8B shows the same data points as a function of the viewing and modified-elevation angles. In both these figures, the normalized spatial OPD_{RMS},

$$OPD_{Norm}\left(\frac{\mu m}{m}\right) = \frac{OPD_{RMS}}{\left(\frac{\rho_0}{\rho_{SL}}\right) M^2 D}, \tag{7}$$

was calculated and the data were interpolated to fill in the appropriate gaps. Note that the units of the normalized OPD_{RMS} are μm/ m.

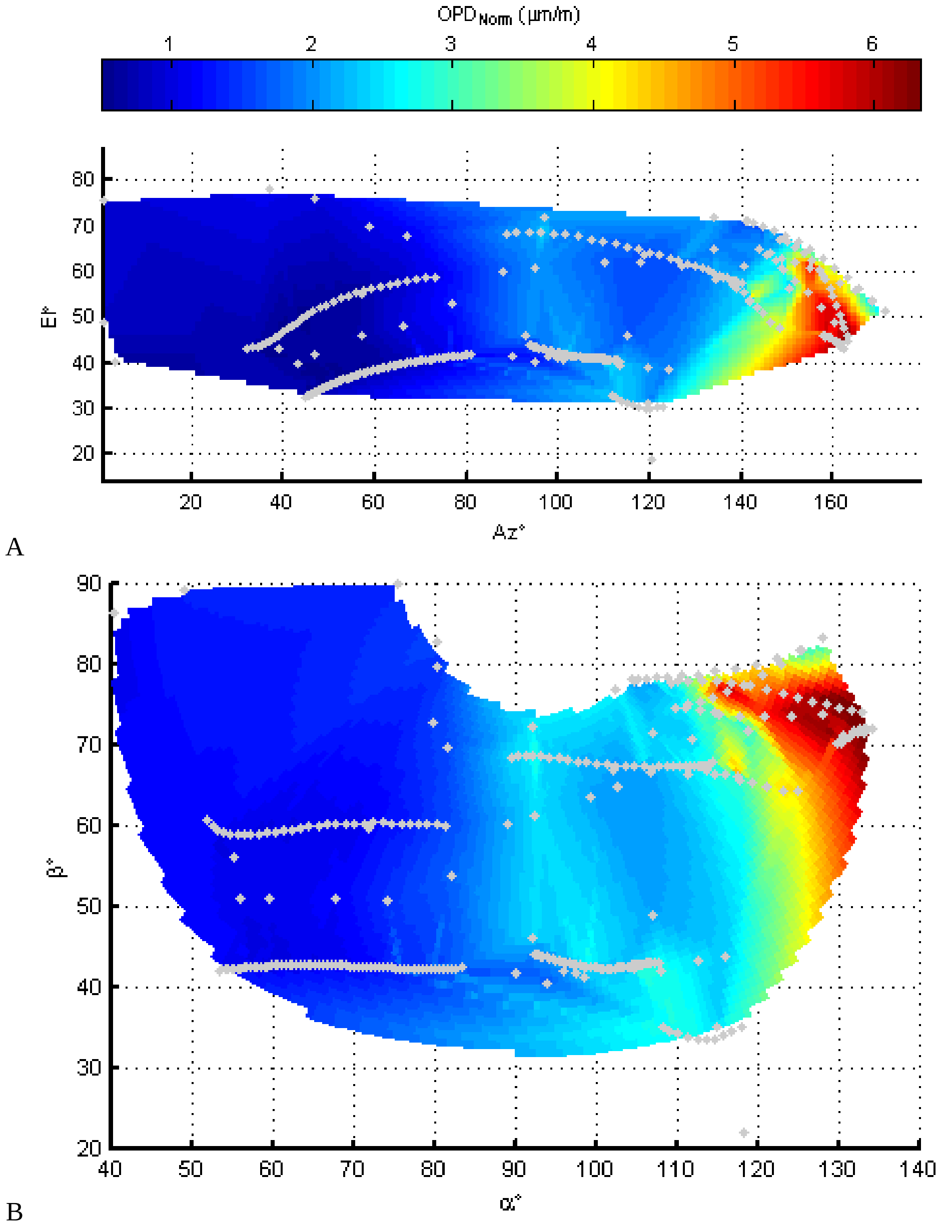

Figure 8. Average normalized spatial OPD$_{RMS}$ as a function of A) the azimuthal and elevation angles and B) the viewing and modified elevation angles.

Analyzing the results in Figure 8, at forward-looking angles, *Az* < 70° or α < 70°, the normalized OPD$_{RMS}$ remained around one, which was comparable with the sensitivity of the wavefront sensor. This indicates that the aero-optical environment at these angles was not largely affected by higher-order aero-optic aberrations. However, beyond an azimuthal (or viewing) angle of 70°, the normalized OPD$_{RMS}$ began to increase reaching a local maximum between 2 and 2.5 at approximately 90 degrees. As shown in Figure 8B, the normalized OPD$_{RMS}$ was only a weak function of the modified elevation angle, β, for viewing angles below 90 degrees; the location of the first peak in the normalized OPD$_{RMS}$ changed by only a few degrees within a range of all modified elevation angles tested. However, in the azimuthal/elevation angle space, the azimuthal location of the first peak changed by roughly 20 degrees over tested elevation angles. This illustrates the usefulness of the viewing-angle space and indicates that ground effects over this range of angles are minimal. After this first peak in the normalized OPD$_{RMS}$, as the viewing angle continued to increase, the normalized OPD$_{RMS}$ began to drop slightly; this phenomenon was attributed to tip/tilt-removal effects and is discussed in detail in [22].

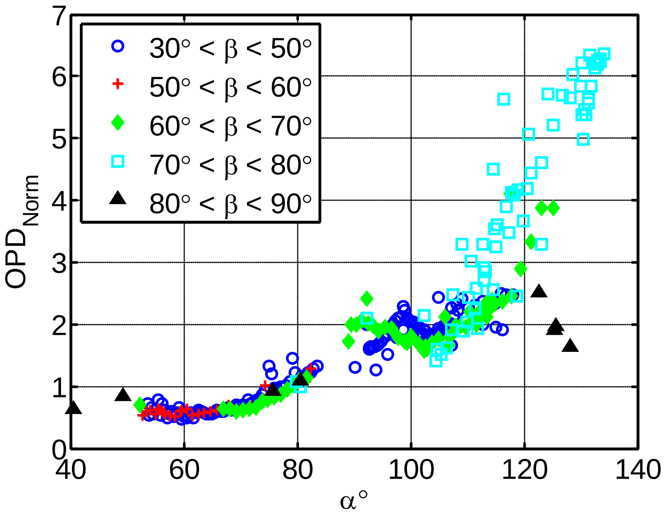

Figure 9. Changes in the normalized OPD as a function of viewing angle for different elevation angle ranges.

For forward-looking angles, the normalized OPD_{RMS} was largely unaffected by ground effects (i.e. modified elevation angle effects), although the location of the first peak shifted slightly as a function of the modified elevation angle. As the viewing angle continued to increase towards 120 degrees, the beam propagated through a larger portion of the wake. Simultaneously, the vortical structures in the wake grew larger in this region of the wake and the normalized OPD_{RMS} increased rapidly, more than doubling over a few degrees. At this range, levels of the aero-optical distortions showed a strong modified-elevation-angle dependence. To better see this dependence, the data were re- plotted in Figure 9 as a function of viewing angle for several narrow ranges of the modified elevation angles. The location of the first local maximum around the viewing angle of 90 degrees is dependent upon the modified elevation angle, implying that the location of the maximum is sensitive to turret ground effects. Also, at the region between $60<\beta<75$ the normalized OPD_{RMS} approached a value of nearly 6 around the viewing angle of 130 degrees, as the modified elevation angle approaches 90 degrees, the normalized OPD_{RMS} dropped to a value of 2. This effect can be explained as follows: near the centerline of the turret, defined as the azimuthal angle of 180 degrees, the beam propagates through a relatively-quiet region of the wake traveling in-between the two horn vortices, as depicted in Figure 3. This is consistent with centerline measurements on a canonical flat-windowed turret [7], along with conformal-window turret tests [5], where normalized levels of aero-optical distortions were around a value of two.

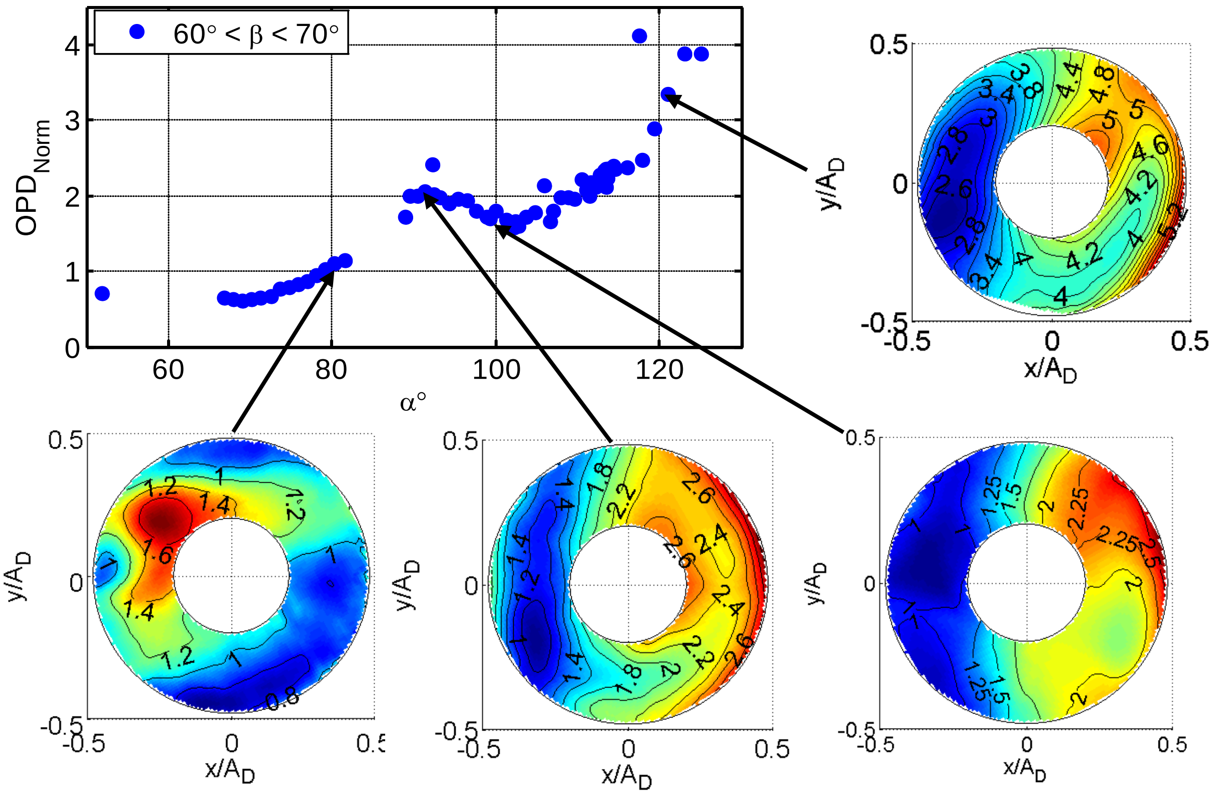

Figure 10. Normalized OPD for the data centered between 60°<β<70° with the corresponding time-average fluctuations across the aperture of the turret.

To help distinguish between optical effects related to the viewing angle and the modified elevation angle, the aero-optical data in the region between 60°<β<70° are shown in Figure 10. In addition, maps of the spatial distribution of temporal variation of the normalized OPD across the aperture are shown for viewing angles of 81°, 92°, 99° and 117°. The flow across the aperture is from left to right. Notice that the temporal variations of the normalized OPD across the aperture are not constant. Except for the 81-degree case, the magnitude of the fluctuations in the upstream portion of the aperture is smaller than the magnitude of the fluctuations in the downstream portion of the aperture. This indicates that as the flow separates from the turret at back-looking angles, the aero-optical structures grow as they propagate downstream, so any wavefront measurements based on the frozen flow hypothesis, like the Malley probe [7], should be treated with caution.

Figure 11 shows instantaneous wavefronts corresponding to four data sets shown in Figure 10. In Figure 11, the scaling in each graph has been adjusted to aid in viewing aberrations in the wavefront. For example, the aberrations shown in Figure 11A are only half as large as the aberrations shown in Figure 11B and 11D. Furthermore, in Figure 11A, the size of the aberrations, relative to the aperture, are smaller and less coherent than the structures seen at the backward-looking angles. In the wavefronts at backward-looking angles, the aberrations appeared as long-spanwise coherent structures resulting from the coherent vortical structures in the shear layer forming around the aperture. Additionally, in Figure 11B, which corresponds to the first peak in the normalized OPD_{RMS}, the upstream portion of the aperture had a local separation bubble that formed from the slope-discontinuity of the flat-windowed aperture. The evidence of this unsteady bubble can also be seen in the spatial distribution plot in Figure 10 for the viewing angle of 91 degrees.

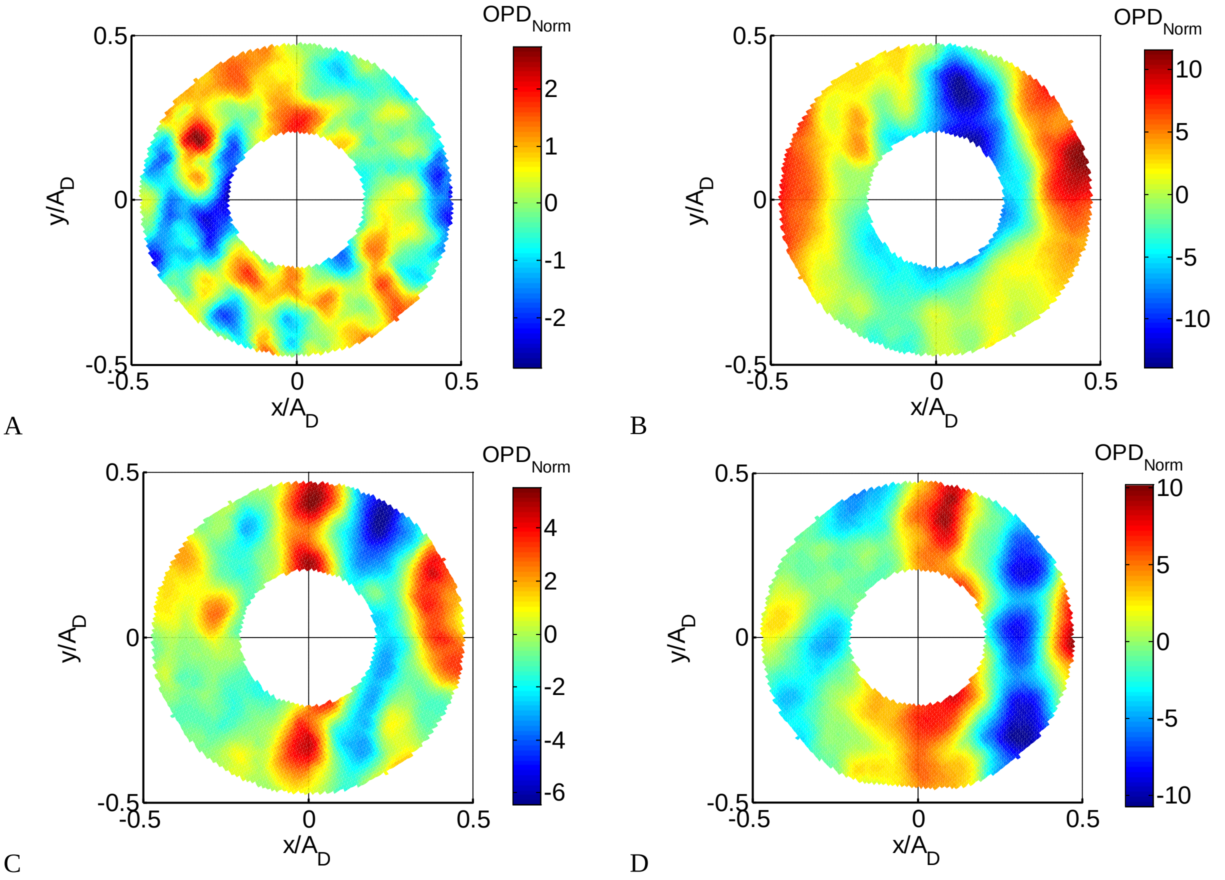

Figure 11. Instantaneous realizations of wavefronts corresponding to viewing angles of A) 81°, B) 92°, C) 99°, and D) 117°. The colormap in each of the figure is adjusted appropriately to aid in the viewing of the types of aberrations present from structures propagating across the aperture.

B. Mach Number Dependence

For the data presented above, all the data was normalized by a scaling factor of $(\rho_0/\rho_{SL})M^2D$. To verify that at sub-transonic Mach numbers this scaling relationship successfully collapsed the data, flight tests were performed at a Mach number of 0.4 and 0.5. The data were acquired at 15,000 ft to assure that the only change in the scaling relationship was the Mach number. Figure 12 shows two data sets on each plot, one at Mach 0.4 and the other at Mach 0.5. Both data sets were acquired over an azimuthal angle range of 145°-160° and an elevation angle range of 45°-67° during their respective slewing maneuvers, so turret-ground and flat-window effects were identical between the two data sets. The top graph shows the unscaled data, in which the magnitude of the aberration at Mach 0.5 is larger than the magnitude of the aberration at Mach 0.4. As shown in the bottom graph, the data successfully collapse onto a single curve when scaled by $(\rho_0/\rho_{SL})M^2D$, verifying the proposed scaling relationship.

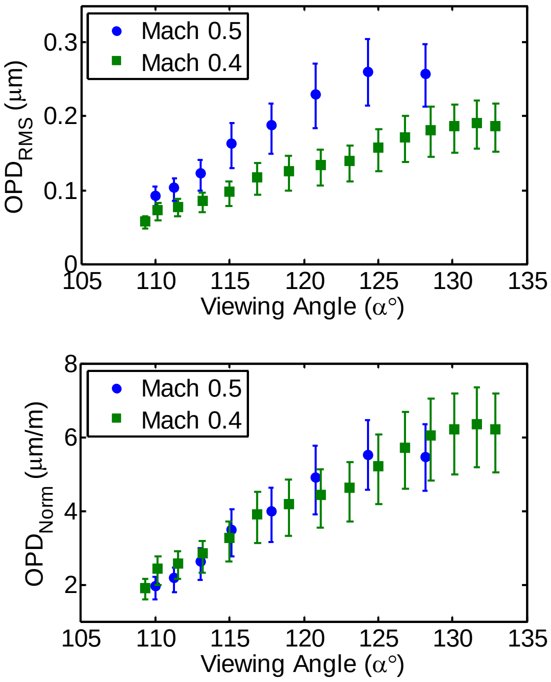

Figure 12. Comparison of optical data at different freestream Mach numbers verifying the proposed scaling relationship of $(\rho_0/\rho_{SL})M^2D$. On the top are the unscaled raw data, and the bottom the scaled data. For each data set, the α and β are within 1-2 degrees of each other

C. Tunnel Data

In addition to the flight tests, aero-optical measurements around the same turret were performed in Notre Dame's 3ft x 3ft wind tunnel to compare the tunnel data with the flight data. The wind tunnel is a closed-loop, temperature controlled wind tunnel. It is capable of freestream Mach numbers up to 0.67 and it has a turbulent intensity below 0.05% [23]. For the tunnel tests, the freestream Mach number was 0.3. Due to the tunnel configuration, all the data presented in Figure 13 is at the elevation angle between 40° and 50° degrees. Figure 13 shows the comparison between wind-tunnel tests and flight tests at comparable range of angles. For both the flight and tunnel tests, the Reynolds number was approximately 2,000,000, which is well above the laminar to turbulent transition range of Re = 300,000 [5].

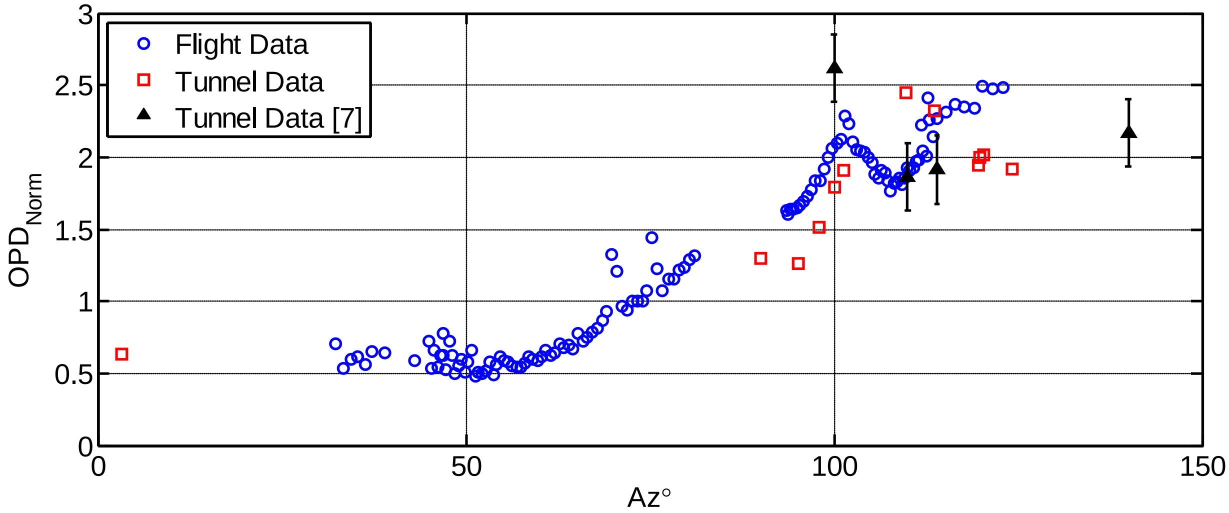

Figure 13. Comparison of flight data and tunnel data on the same turret along with previous optical data from a different turret [7]. All the AAOL data shown is for β<45°.

As shown in Figure 13, the normalization of the data collapses both the tunnel and the flight data to similar nominal values. The azimuthal angle of the first local maximum has shifted from approximately 110 degrees for the flight data to a smaller value of 100 degrees in the tunnel-tests. The reason of the shift in the peak is currently being investigated, but it is probably related to the wake separating from the turret earlier during flight then in the tunnel because of tunnel-blockage effects. Similar results have been seen in *Cp* data where large tunnel blockage values have kept the flow attached up to 130 degrees [5]. Given the difference in the elevation angle and blockage effects, the normalized data from the tunnel tests and from the flight tests match fairly well and the existing differences are mostly within the error of the measurements.

In Figure 13, the results of the tunnel tests taken at the Air Force Academy subsonic tunnel are also presented [7]. The amplitude of the normalized OPD_{RMS} agreed well with both flight tests and Notre Dame tunnel tests. The small difference between the Air Force Academy tunnel test and the Notre Dame tunnel tests can be contributed to a slightly different geometry of the flat-window turret. The turret used in the Academy-tunnel was a canonical hemisphere-on-cylinder turret, while the AAOL turret has a cutout in the cylindrical portion of the turret and small gaps between the rotating and the stationary parts of the turret, see Figure 4.

D. Structure Size and Correlation of the Data

Both streamwise and spanwise correlation lengths can be obtained by auto-correlating wavefronts. Figure 14 shows an normalized-autocorrelation map and the corresponding slices through the correlation map at $\Delta y/A_D = 0$ and $\Delta x/A_D = 0$; the data shown is at an azimuthal angle of 134° and an elevation angle of 65°. Using the definition of the correlation length as the location of the first minima, the structure size in this case was 0.67R, where R is the radius of the aperture. This result is larger than the correlation lengths reported in [7], although the Mach number and viewing angle were different in this case; furthermore, one-dimensional wavefronts were measured in [7] using a Malley probe so spanwise effects were not captured. Concentrating on the fixed-angle data between $60° < \beta < 70°$, the structure size was calculated for the various viewing angles and results are presented in Figure 15. The structure size, defined as a location of the first minima in the streamwise direction, decreases as the viewing angle increases until it levels out around 93 degrees. This location corresponds to the angle at which the normalized OPD_{RMS} reaches the first local maxima at these modified elevation angles.

Using the time-resolved wavefront data, the convective velocity of optical structures can be calculated one of two ways: by spatially cross-correlating time-delayed wavefronts over the entire aperture or by calculating the phase slope as a function of the frequency, similar to the Malley probe analysis [7]. Figure 16 shows the average calculated velocity of the optical structures based on the first estimate. Depending on the time difference between the wavefronts being correlated, the optical structure velocity varied slightly. However, for all the cases, the structures were primarily propagating in the streamwise direction across the aperture at a velocity of approximately 0.95 of the freestream velocity. Similar values were reported in [7]. Note that the local flow speed over the aperture is larger than the freestream velocity by approximately a factor of 1.5 due to the turret blockage. Therefore, the convective velocity was approximately 0.6 of the local flow velocity over the aperture. This value is consistent with the normalized convective speed of large-scale structures within shear layers and has been observed experimentally at back-looking angles in other tests [7, 22].

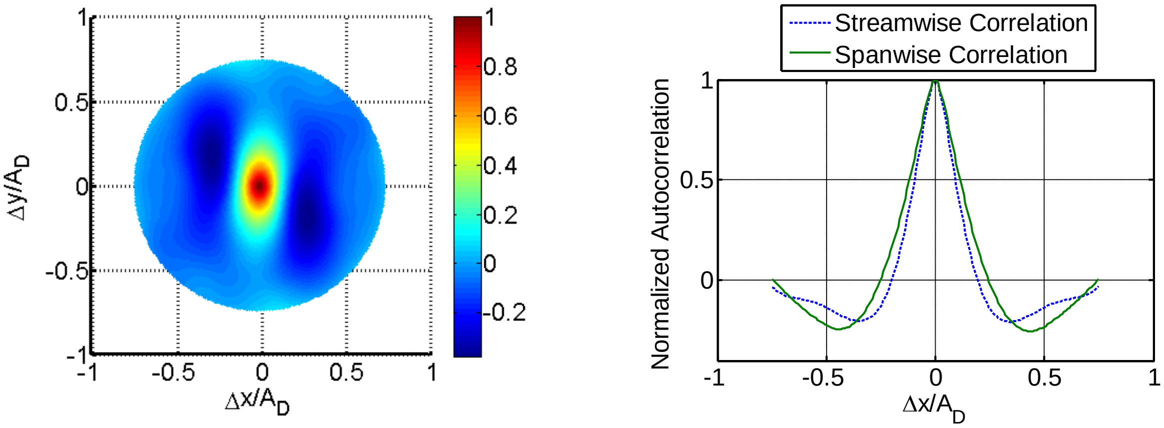

Figure 14. Normalized auto-correlation of OPD at Az = 134°, El = 65°.

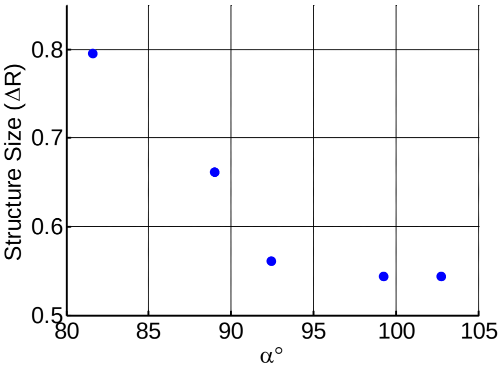

Figure 15. The calculated structure size from auto correlating wavefront data for 60°<β<70°.

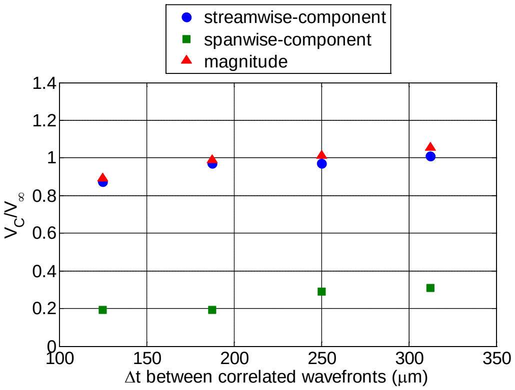

Figure 16. Calculated velocity by correlating wavefronts using different time delays between wavefronts at a flight speed of Mach 0.5.

E. Far Field Implications

While all the data presented above were quantified by calculating the spatial OPD_{RMS} across the aperture for different azimuthal and elevation angles, the primary aero-optic concern is the reduction of the far-field irradiance delivered to target as a result of these aberrations, typically quantified by the instantaneous or time-averaged Strehl ratio. As mentioned in Section IIB, if the spatial distribution in the instantaneous wavefront error is Gaussian, the OPD_{RMS} using Eq. (5a) accurately predicts the instantaneous Strehl ratio. Therefore, the question remains as to whether or not the wavefront data resulting from aero-optic aberrations meet this criterion. Figure 17 shows histograms of the calculated instantaneous spatial statistics of a given data set at a viewing angle of 104°. In the figure, three histograms are shown corresponding to the normalized OPD_{RMS} (left), the skewness (center), and the excess (right), where the skewness and excess are defined as:

$$\gamma_1 = E\left[\frac{X-\mu}{\sigma}\right]^3 = \frac{\mu_3}{\sigma^3} \tag{8}$$

$$\gamma_2 = E\left[\frac{X-\mu}{\sigma}\right]^4 - 3 = \frac{\mu_4}{\sigma^4} - 3. \tag{9}$$

In Eqs. (8) and (9), X is a random variable (OPD in this case), μ_3 is the third moment about the mean, μ_4 is the forth moment about the mean, σ is the standard deviation or OPD_{RMS}, and E is the expectation operator. When the probability distribution function of the instantaneous spatial wavefront error is Gaussian, the skewness and excess are exactly zero. Nevertheless, as seen in Figure 17, a large number of the instantaneous wavefronts do not have the skewness or the excess of zero.

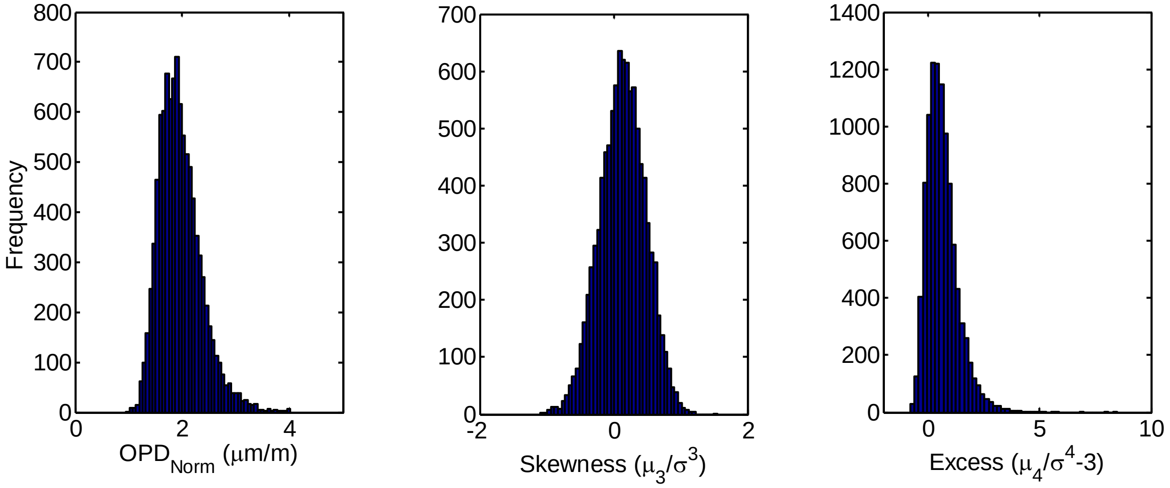

Figure 17. Histograms of the normalized spatial OPD_{RMS} (left), skewness (middle), and Excess (right) showing the distribution of values at a viewing angle of 104°.

Figure 18 shows the calculated normalized OPD_{RMS}, the skewness, and the excess as a function of the viewing angle (for all modified elevation angles). The spread of the normalized OPD_{RMS}, skewness, and excess for each data point was defined using the Cumulative Distribution Function, CDF, from the corresponding probability distribution functions, PDF(t),

$$CDF(X) = \int_{-\infty}^{X} PDF(t)dt. \tag{10}$$

To define the spread, the points where the CDF equaled 0.25 and 0.75 were calculated; these values result in a spread slightly larger than plus or minus one standard deviation from the mean. Error bars on each of the graphs are used to represent the spread in the data. Note that while experimental error results in additional scatter in the data, the primary cause of the spread is from aero-optical structures propagating across the aperture.

At forward-looking angles ($\alpha < 60°$), the average skewness and the excess are nearly zero. As shown in Figure 11A, the high-order wavefront error consists of small-incoherent structures probably resulting from the boundary-layer present on the forward portion of the turret. Within this viewing angle range, the wavefront error distribution is nearly Gaussian and the exponential form of the Maréchal approximation, Eq. (5a), accurately predicts the instantaneous Strehl ratio. As the viewing angle increases past 60 degrees, the slope discontinuity from the flat-window aperture causes a local flow separation bubble to form. At this point, the normalized OPD_{RMS} begins to increase as coherent vortical structures form across the aperture (Figure 11B-C). Since the wavefront error is the result of coherent vortical structures, the probability distribution function of the OPD across the aperture in no longer Gaussian and the average skewness values become negative with a corresponding positive excess. Finally, as the viewing angle increases past approximately 110 degrees (Figure 11D), although large coherent structures can be seen in the wavefronts, the average skewness and excess return to zero and the probability distribution function of the OPD is Gaussian. However, note that as shown by the spread, instantaneous values of the skewness and excess can drop below zero as these vortical structures propagate across the aperture.

To see how the probability distribution function of the wavefront error affects the instantaneous Strehl ratio, an alternative formulation [2] of Eq. (6) yields the instantaneous Strehl ratio based on the probability distribution function (PDF) of the OPD:

$$SR(t) = \left| \int_{-\infty}^{\infty} e^{\left(2\pi i OPD/\lambda\right)} PDF(OPD)dOPD \right|^2 = |\phi(2\pi/\lambda)|^2, \tag{11}$$

where ϕ is the characteristic function, or the Fourier transform of the PDF. For example, the characteristic function of a Gaussian distribution is

$$\phi(2\pi/\lambda) = e^{im(2\pi/\lambda) - \frac{\sigma^2(2\pi/\lambda)^2}{2}}, \tag{12}$$

where *m* is the mean (which is zero by definition, Eq. (4)) and σ is the instantaneous OPD_{RMS}; substituting Eq. (12) into Eq. (11) recovers the Maréchal approximation, Eq. (5a). For non-Gaussian distributions, the far-field Strehl ratio depends on the high-order moments of wavefronts.

To illustrate the effect of non-Gaussian probability distributions, Figure 19 shows the calculated the Strehl ratio from forward- (left plot) and backward- (right plot) looking angles. The instantaneous Strehl ratio, shown as dots in Figure 19 was calculated using the Fraunhofer approximation, Eq. (6), for a range of wavelengths. The time-averaged Strehl ratio, for a given wavelength, from the instantaneous Fraunhofer-calculated Strehl ratio is shown as a dotted line in Figure 19. Furthermore, the Strehl ratio was calculated with the LAA, Eq. (5b), using the time-averaged OPD_{RMS} and is plotted as a solid line in Figure 19. At the forward-looking angle shown, the phase error distribution was nearly Gaussian, and the difference between the actual Strehl ratio and LAA is small, although the LAA consistently under-predicts time-averaged Strehl ratios. At the backward-looking angle, the difference between the correct Strehl ratio and the LAA predictions is even worse. In addition, the instantaneous Strehl ratios have a lot of scatter, which is completely missed using the LAA.

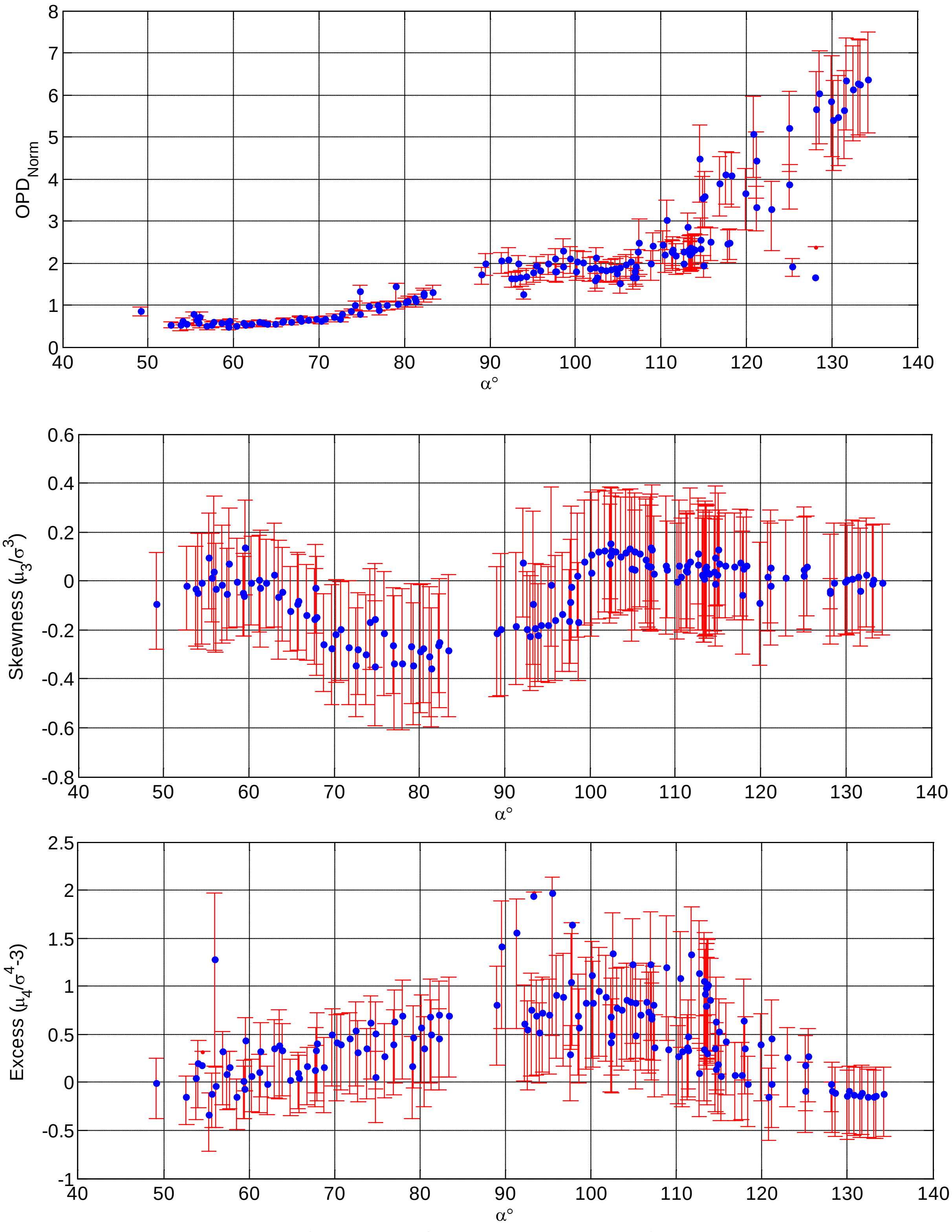

Figure 18. High-order statistics of all the wavefront data over a range of viewing angles. The normalized OPD (top), skewness (center), and excess (bottom) are shown.

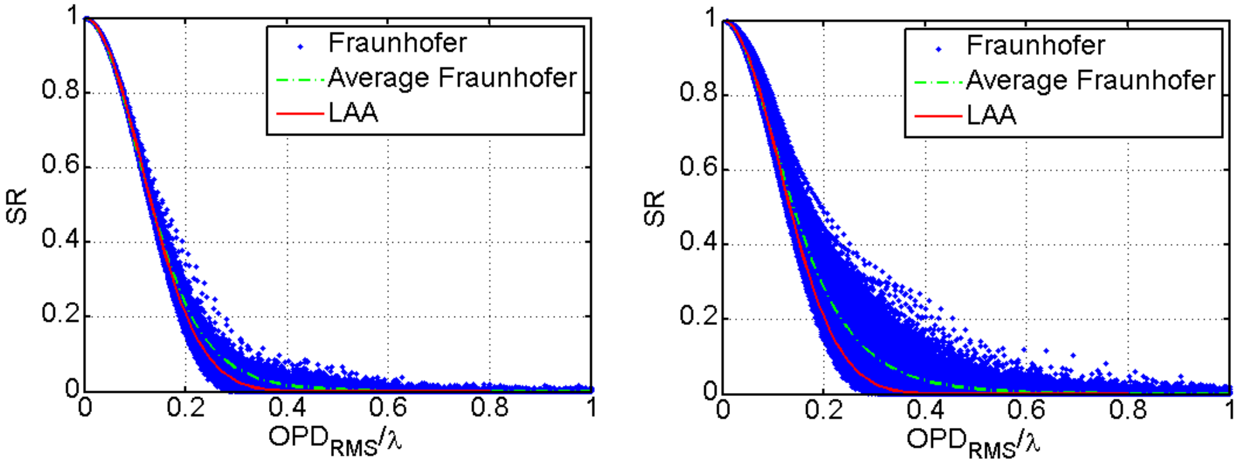

Figure 19. Comparison of the calculated Strehl ratio using the instantaneous wavefronts with the Fraunhofer approximation, the average Strehl ratio using the Fraunhofer approximation, and the LAA based on the average OPD$_{RMS}$/λ at a viewing angle of 60° (left) and 96° (right).

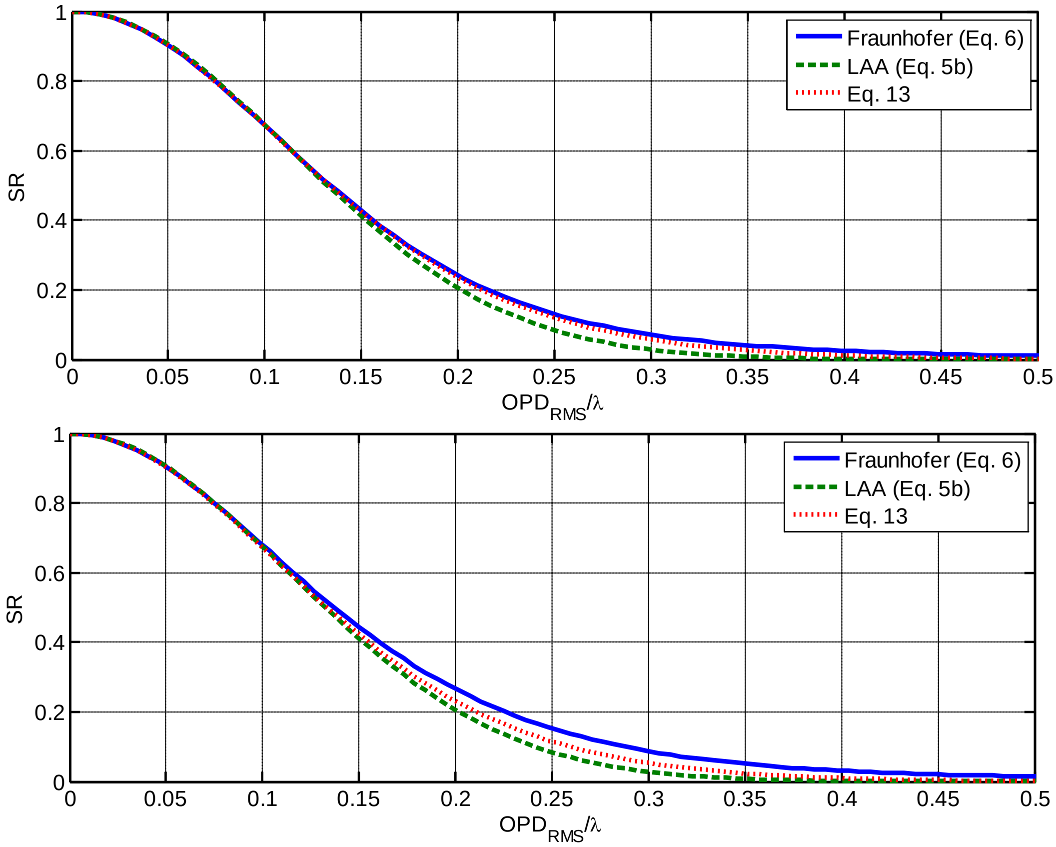

Figure 20. Time-averaged Strehl ratio using various equations at two different angles: top) Az = 108° and El = 60° and bottom) Az = 119° and El = 57°.

In addition to the Gaussian requirements, the Maréchal approximation, Eq. (5a), applies only to instantaneous data. However, sometimes the LAA, (Eq. (5b)), which is only an approximation, is used to calculate the time-averaged Strehl ratio. It is easy to see that even if the spatial distribution of the OPD is Gaussian at every instance, the OPD$_{RMS}$ for finite apertures varies in time, as shown in the left plot of Figure 17. However, using the time-averaged operator inside the non-linear exponential function in Eq. (5b) is not correct. Instead, it is easy to show the correct expression to calculate the time-averaged Strehl ratio for a stationary Gaussian process is,

$$\overline{SR} = \int \exp\left[-(2\pi OPD_{RMS}/\lambda)^2\right] PDF(OPD_{RMS})\, d(OPD_{RMS}) \tag{13}$$

where PDF(OPD$_{RMS}$) is the PDF of the OPD$_{RMS}$(t).

Figure 20 shows a comparison of the computed time-averaged Strehl ratio using the Fraunhofer approximation, Eq. (6), Eq. (13), and the LAA, Eq. (5b), for two angles. At an azimuthal angle of 108° and an elevation angle of 60°, the mean excess was 0.1663, while at an azimuthal angle of 119° and an elevation angle of 57°, the mean excess was 0.6102. As shown in the top plot in Figure 20, when the mean excess is small and the process is approximately Gaussian, the Fraunhofer approximation, Eq. (6), and the correct time-averaged Strehl ratio for Gaussian processes, Eq. (13), provide nearly the same results; the LAA always under-predicts the time-averaged Strehl ratio. When the process is not Gaussian, the bottom plot in Figure 20 shows that both Eq. (13) and the LAA provide inaccurate estimation of the time-averaged Strehl ratio, although Eq. (13) still provides a better estimate of the correct time-averaged Strehl ratio.

V. Conclusions

This paper presents the results of the extensive measurements of the complex aero-optical environment around the side-mounted, flat-window turret performed in-flight using AAOL. Prior to this set of data, optical-experimental data of the aero-optical environment around a flat-windowed turret in open literature were very sparse, with the largest published data set consisting of only four data point. Furthermore, all data up to this point have been obtained either in a wind tunnel or computationally. AAOL provides a unique capability to collect large amounts of flight data during relatively-short flight sequences. Using a high-speed wavefront sensor on board of AAOL allows acquiring wavefronts at different azimuthal/elevation angles with good spatial and temporal resolution. To analyze the data, a different frame of reference, the viewing and modified-elevation angles was proposed. In this frame of reference, differences in optical data at a fixed viewing angle can be directly attributed to ground effects and asymmetries in the wake around the turret. Results showed that aero-optical aberrations are negligible for small forward-looking viewing angles less than 70 degrees. Above 70 degrees, a small separation bubble appeared at the front edge of the flat window, introducing convecting, small-scale structures over the aperture and causing aero-optical distortions to increase. The aero-optical levels have a local peak around the viewing angle between 90 and 100 degrees, followed by a small drop in the levels in the range of viewing angles between 100 and 110 degrees. Above these viewing angles, aero-optical aberrations increase sharply with the viewing angle, except for the region aft of the turret near the center plane with the azimuthal angle around 180 degrees, where the levels stayed approximately constant or even decreased. All of these results were found to be consistent with the flow topology features around the turret. Data sets in flight at different Mach numbers showed that the scaling relationship normalizing low subsonic optical data by $(\rho/\rho_{SL})M^2D$ successfully captured the Mach-number dependence. Finally, flight results were compared to tunnel data results and differences were discussed.

In addition to the root-mean-squared levels of aero-optical distortions, higher-order spatial statistics were calculated and their dependence as a function of the viewing angle was discussed. Given the optical data obtained, the applicability of the commonly-used Large Aperture Approximation was revisited. It was shown that for all angles the LAA consistently under-estimates the time-averaged Strehl ratio, so the LAA should be used very cautiously. Some reasons for these discrepancies were traced to non-Gaussian spatial distribution of the optical wavefronts. Other approximations to compute both the instantaneous and time-averaged Strehl ratios were considered and the results were discussed.

The future flight tests will expand the envelope of the measured azimuthal/elevation angles and will also include transonic speeds to better understand the aero-optical environment around the turret.

Acknowledgments

The authors would like to thank the Northern Air personnel, especially Kevin Tessmer for providing technical assistance during flight test. We would also like to thank Matthew Krizo from AFIT for providing assistance on the laser tracking system.

These efforts were sponsored by the High Energy Laser Division of the Joint Technology Office (HEL JTO) and supported by the Air Force Office of Scientific Research, Grant number FA9550-07-1-0574. The U.S. Government is authorized to reproduce and distribute reprints for governmental purposes notwithstanding any copyright notation thereon.

References

[1] Duffner, R., (2009). The Adaptive Optics Revolution: A History, *University of New Mexico Press,* 202-235.
[2] Ross, T. S. (2009). Limitations and applicability of the Maréchal approximation, *Applied Optics*, 48(10), 1812-1818.
[3] Butts, R., and Weaver, L. D., (1994). Airborne laser experiment (ABLEX): theory and simulations, *SPIE – Laser beam propagation and control*, 2120(10).
[4] Weaver, L. D., and Butts, R., (1994). ABLEX: High altitude laser propagation experiment, *SPIE – Laser Beam Propagation and Control*, 2120(30).
[5] Gordeyev, S., and Jumper, E. J., (2010). Fluid dynamics and aero-optics of turrets. *Prog. Aerospace Sci.* (2010), 46, 388-400.
[6] Gordeyev, S., Cress, J. A., Smith, A., and Jumper, E. J., (2010). Improvement in Optical Environment over Turrets with Flat Window Using Passive Flow Control, AIAA-2010-4492, 41st AIAA Plasmadynamics and Lasers Conference, 28 Jun-1 Jul, 2010, Chicago IL.
[7] S. Gordeyev, T. Hayden and E. Jumper, **"**Aero-Optical and Flow Measurements Over a Flat-Windowed Turret**"**, *AIAA Journal*, vol. **45**, No. 2, pp. 347-357, 2007.
[8] Ladd, J., Nani, M., and Bower, W., Validation of Aerodynamic and Optical Computations for the Flow about a Cylindrical/Hemispherical Turret, AIAA 2009-4118, 2th AIAA Applied Aerodynamics Conference, 22-25 June, 2009, San Antonio, TX.
[9] Pond, J. E., and Sutton, G., Aero-optic Performance of an Aircraft Forward-Facing Optical Turret, Journal of Aircraft, Vol. 43, No. 3, May-June 2006.
[10] Morgan, P. E., and Visbal, M. R., Large Eddy Simulation of Flow Over a Flat-Window Cylindrical Turret with Passive Flow Control, AIAA 2010-916, 48th AIAA Aerospace Sciences Meeting, 4-7 January, 2010, Orlando FL.
[11] White, M. D., Morgan, P. E., and Visbal, M. R., High Fidelity Aero-Optical Analysis, AIAA 2010-433, 48th AIAA Aerospace Sciences Meeting, 4-7 January, 2010, Orlando FL.
[12] Zenk, M. A., Wang, M., Jumper, E. J., Cusumano, S., Maple, R., Whiteley, M. and Widiker, J., The Airborne Aero-Optics Laboratory: The Use of Simulation and Modeling in Its Development, Directed Energy Systems Symposium, 3-7 March 2008, Monterrey, CA.
[13] Fitzgerald, E.J., and Jumper, E.J., (2004). The optical distortion mechanism in a nearly incompressible free shear layer. *Journal of Fluid Mechanics*, 512, 153-189.
[14] Rennie, R.M., Duffin, D.A., and Jumper, E.J., (2008). Characterization and aero-optic correction of a forced two-dimensional weakly compressible shear layer, *AIAA Journal,* 46(11), 2787-2795.
[15] Zubair, F. R., Freeman, A. P., Piatrovich, S., Shockro, J., Ibrahim, Y., N., and Catrakis, H., J., Large Scale Turbulence Suppression Control for Direct Reduction of Aero-Optical Aberrations, AIAA 2007-4008, 38th Plasmadynamics and Lasers Conference, 25-28 Jun, Miami, FL.
[16] Catrakis, H. J., and Aguirre, R. C., New Interfacial Fluid Thickness Approach in Aero-Optics with Applications to Compressible Turbulence, AIAA Journal, Vol. 42, No. 10, October 2004.
[17] Cress, J.A., Gordeyev, S., Post, M.L., and Jumper, E.J., (2008). Aero-optical measurements in a turbulent, subsonic boundary layer at different elevation angles, *AIAA paper 2008-4214*.
[18] Stine, H. A., and Winovich, W. (May 1954). Light diffusion through high-speed turbulent boundary layers. Research Memorandum A56B21, NACA, Washington.
[19] C. M. Wyckham and A. J. Smits. Aero-optic distortion in transonic and hypersonic turbulent boundary layers. *AIAA Journal*, 47(9):2158–2168, Sep 2009.
[20] Wallace, R. D., Shea, P. R., Glauser, M. N., Vaithianathan, T., and Carlson, H. A., Feedback Flow Control for a Pitching Turret (Part II), AIAA 2010-361, 48th AIAA Aerospace Sciences Meeting, 4-7 January, 2010, Orlando FL.
[21] Steinmetz WJ, (1982) Second Moments of Optical Degradation Due to a Thin Turbulent Layer. In *Aero-Optical Phenomena, Progress in Astronautics and Aeronautics,* Vol. 80, ed. KG Gilbert, LJ Otten, pp. 78-110. New-York:AIAA.
[22] S. Gordeyev, J.A. Cress, E. Jumper and A.B. Cain, "Aero -Optical Environment Around a Cylindrical Turret with a Flat Window", *AIAA Journal*, Vol. **49**, No. 2, pp. 308-315, 2011.
[23] J. A. Cress, *Optical Distortions Caused by Coherent Structures in a Subsonic Compressible, Turbulent Boundary Layer*, Ph.D Thesis, University of Notre Dame, 2010.